Article

CoPi/Co(OH)$_2$ Modified Ta$_3$N$_5$ as New Photocatalyst for Photoelectrochemical Cathodic Protection of 304 Stainless Steel

Xuan Xie [1,2] [ID]**, Li Liu [1,2,*], Emeka E. Oguzie [3], Ying Li [2] and Fuhui Wang [1,2]**

[1] Shenyang National Laboratory for Materials Science, Northeastern University, NO. 3-11, Wenhua Road, Heping District, Shenyang 110819, Liaoning, China; xxie14s@imr.ac.cn (X.X.); fhwang@imr.ac.cn (F.W.)

[2] Institute of Metal Research, Chinese Academy of Sciences, 62# Wencui Road, Shenyang 110016, Liaoning, China; liying@imr.ac.cn

[3] Electrochemistry and Materials Science Research Laboratory, Department of Chemistry, Federal University of Technology Owerri, Owerri PMB 1526, Nigeria; oguziemeka@yahoo.com

* Correspondence: liliu@imr.ac.cn

check for updates

Abstract: In this work, CoPi and Co(OH)$_2$ nanoparticles were deposited on the surface of Ta$_3$N$_5$ nanorod-arrays to yield a novel broad-spectrum response photocatalytic material for 304 stainless steel photocatalytic cathodic protection. The Ta$_3$N$_5$ nanorod-arrays were prepared by vapor-phase hydrothermal (VPH) and nitriding processes and characterized by scanning electron microscopy (SEM), X-ray diffraction (XRD), X-ray photoelectron spectroscopy (XPS), and UV-Vis spectroscopy, respectively, to obtain morphologies, crystal structures, surface compositions, and light response range. In order to analyze the performance improvement mechanism of CoPi/Co(OH)$_2$ on Ta$_3$N$_5$ nanorod-arrays, the electrochemical behavior of modified and unmodified Ta$_3$N$_5$ was obtained by measuring the open circuit potential and photocurrent in 3.5 wt% NaCl solution. The results revealed that the modified Ta$_3$N$_5$ material better protects 304 stainless steel at protection potentials reaching -0.45 V.

Keywords: Ta$_3$N$_5$ nanorod-arrays; CoPi/Co(OH)$_2$ modification; cathodic protection; photocatalysis

1. Introduction

Since Fujishima and Honda [1] first reported the photoelectric effect of TiO$_2$ in 1972, photocatalytic materials have become increasingly important, with diverse applications in several industrial processes [2–6]. Research has shown that many common photocatalytic materials, such as TiO$_2$ [5,7], ZnO [8,9], and SnO$_2$ [10], have wide band gaps, which means that they have almost only ultraviolet light response and have a low utilization rate of sunlight in practical applications. What's more, it is difficult for a single photocatalyst to function effectively independently, even for rather simple processes like decomposition of water. In the same vein, single photocatalyst materials do not function efficiently in electrochemical protection applications. Photocatalytic activity can often be improved by regulating crystal surface [11] and surface defects [12], as well as by noble metal deposition [13,14] or semiconductor combination [15,16], which often result in photocatalytic composite systems with improved performance. Another approach involves exploration, design, and development of novel photocatalytic materials.

Some recent studies have focused on developing a new class of photocatalytic materials that respond readily to a broad range of spectra and can make full use of visible light to achieve photocatalysis. A material like BiVO$_4$, for instance, with a band gap of 2.4 eV, has a large visible region response and successfully degrades organics in visible light [17].

Ta_3N_5 is a novel photocatalytic material with a broad spectral response range [18–21]. Ta_3N_5, prepared by Hara et al. [22], could oxidize water into O_2 efficiently, with maximum quantum yields of 10%. Luo et al. [23] reported that in the visible region nano Au/Ta_3N_5 composite showed a significantly enhanced photocatalytic activity for hydrogen evolution from water. Zhen et al. [24] reported that a Ta_3N_5 nanorod modified with $Co(OH)_x$ had a strong absorption in the visible light range up to 620 nm and could achieve high photon-to-current conversion efficiency. The use of catalyst promoters like $Co(OH)_x$ [25,26] and CoPi [27,28] has become an important and promising way to improve the photocatalytic capability of photocatalysts [29–33]. Such promoters function by restraining the recombination rate of interfacial photogenerated electron-hole pairs and play a useful role in providing ready sites for the oxidation half reaction [34].

In the 1990s, Tsujikawa and Yuan [5] first proposed a TiO_2 photocatalytic coating technique for cathodic corrosion protection of carbon steel. Since then, the use of photocatalysts in cathodic protection has continued to attract attention within the scientific community and different photocatalytic materials have been investigated for metal corrosion protection efficacy. Sun et al. [35] reported that a C_3N_4-In_2O_3 nanocomposite with quasi-shell-core structure provides photoelectrochemical cathodic protection for the coupled 304 stainless steel (SS) under visible light. Wang et al. [36] observed that Bi_2Se_3/TiO_2 nanocomposites successfully exhibited great photogenerated cathodic protection performance for 304 stainless steel.

However, we have not seen any reports on the use of Ta_3N_5 materials for photoelectrochemical cathodic protection of metals. Compared to the previous work on Ta_3N_5, it is necessary and meaningful to explore the cathodic protection performance of this material with a broad spectral response range.

In this work, a vapor-phase hydrothermal process and subsequent nitriding treatment were used to prepare Ta_3N_5 nanorod-array films, which were subsequently modified by addition of $CoPi/Co(OH)_2$ and subjected to microstructure characterization. The change of photoelectrochemical cathodic protection properties of Ta_3N_5 material before and after modification were compared using electrochemical methods. This study provides a theoretical basis for the application of novel photocatalytic materials with broad spectral response ranges in cathodic protection.

2. Experimental Section

2.1. Specimen Preparation and Modification

Vapor-phase hydrothermal (VPH) is a process to grow metal oxides on the corresponding metal matrix, which has become a very attractive method in recent years [37,38]. It has been used in growth of ZnO nanotube and nanorod-array films on a zinc foil substrate [37] and growth of rutile nanorod and titanate nanotubes on a titanium foil substrate [38].

In this work, based on previous methods, one-dimensional Ta_2O_5 nanorod-arrays were synthesized on a tantalum foil substrate (10 mm × 15 mm) by the VPH process, and these arrays were subsequently converted to Ta_3N_5 nanorod-array films by NH_3 nitriding treatment [24].

To obtain the Ta_3N_5 material modified by $CoPi/Co(OH)_2$, double co-catalysts, CoPi and $Co(OH)_2$, were deposited as follows: CoPi was loaded on the surface of Ta_3N_5 nanorod-array films by photoelectric chemical deposition [28], and then $Co(OH)_2$ was modified by chemical deposition modification on top of CoPi [24].

2.2. Characterization of Ta_3N_5

The surface morphologies of the Ta_3N_5 nanorod-array films were observed and analyzed using an INSPECT F50 (FEI Co., Hillsboro, OR, USA) field emission scanning electron microscope (SEM), while the growth thickness of the films was also observed by cross-section morphologies at a working voltage of 25 kV. The crystalline structures were measured through a X'pert PRO (Panalytical, Almelo, The Netherlands) X-ray diffractometer (XRD) using Cu Kα radiation at 40 kV, with 2θ ranging from 10° to 90°. In order to identify if $CoPi/Co(OH)_2$ was successfully loaded, the changes of surface

elemental compositions were analyzed by ESCALAB250 (Thermo VG, Waltham, MA, USA) X-ray photoelectron spectroscopy (XPS) with Al Kα radiation. The ultraviolet-visible spectra of the Ta_3N_5 films were collected by a diffuse reflectance V-770 (JASCO, Tokyo, Japan) UV-Vis spectrophotometer in the wavelength range 200–900 nm.

2.3. Preparation of Ta_3N_5 Electrode

The Ta_3N_5 nanorod-array films were fabricated into electrodes before use in photoelectrochemical performance tests for metal protection. The Ta_3N_5 electrode and 304 stainless steel electrode were cut in the same size (10 mm × 15 mm). One side of each sample was exposed to the corrosive solution and the other sides covered with a resin-paraffin mixture (1:1). The samples were pasted and fixed to copper wires as electrodes. A 3.5 wt% NaCl solution was used as electrolyte solution in order to simulate the seawater environment.

2.4. Characterization of Photoelectrochemical Performance

Characterization of photoelectrochemical performance was conducted using a PGSTAT302N potentiostat Autolab (Metrohm Autolab, Utrecht, The Netherlands). As shown in Figure 1a, a Pt electrode and a KCl-saturated silver/silver chloride electrode (Ag/AgCl) were connected as counter electrode and reference electrode, respectively. The Ta_3N_5 electrodes with and without $CoPi/Co(OH)_2$ modification were coupled with 304 stainless steel and used as working electrodes. This connection method enabled detection of the open circuit potential (OCP) changes over time in the dark and under illumination, respectively.

The electrochemical noise module (ECN) was used to measure the photogenerated current of the two kinds of Ta_3N_5 electrodes as a function of time, in the dark and under illumination. As shown in Figure 1b, the working electrode Ta_3N_5 was placed opposite the 304 stainless steel counter electrode (connected to the ground wire in ECN measurements, so that electrons can flow from the Ta_3N_5 electrode to the 304 stainless steel electrode); the Ag/AgCl electrode was connected likewise as reference electrode. All the measured potentials were relative to the Ag/AgCl electrode (0.1981 V). The electrolyte, 3.5 wt% NaCl solution, was replaced for each new measurement. The light source was a 300 W PLS-SXE 300 Xe lamp (Beijing PerfectLight Co. Ltd., Beijing, China). The experimental temperature was at room temperature.
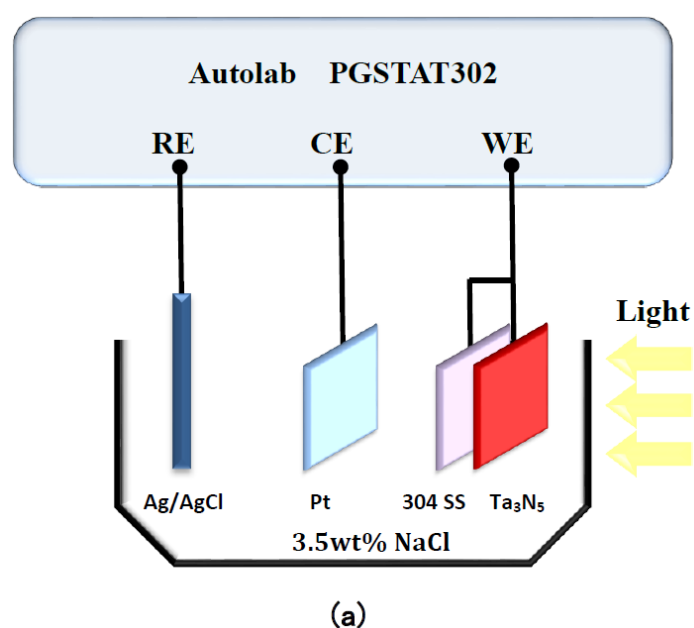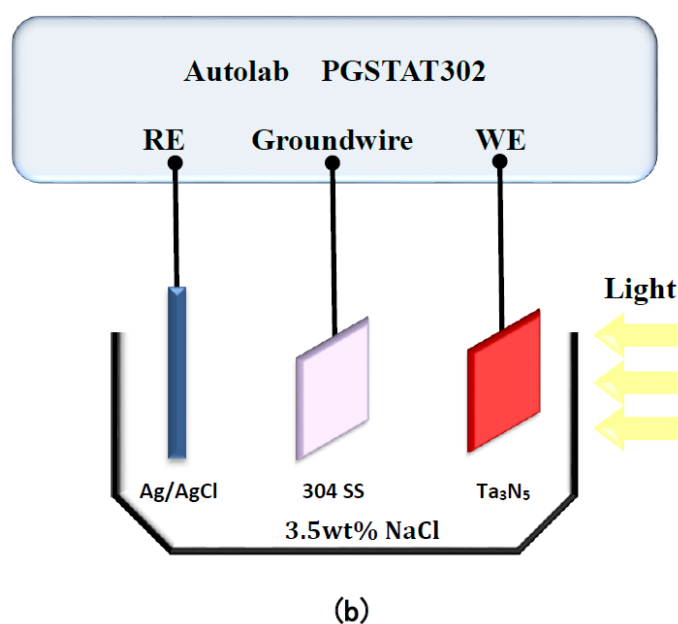

(a)

Figure 1. *Cont.*

(b)

Figure 1. Schematic diagram of the Autolab electrochemical test system for measuring (**a**) open circuit potentials and (**b**) photocurrent densities of Ta₃N₅ films.

3. Results and Discussion

3.1. Micromorphologies of Ta₃N₅

The macroscopic surface of the Ta₃N₅ material prepared by the VPH method and nitriding treatment was a uniform and wine-red film. The micromorphologies of the unmodified Ta₃N₅ (shown in Figure 2) grew in the form of a vimineous nanorod-array, continuously and closely connected to each other (Figure 2a). The corresponding cross-section morphology shows the nanorod-arrays to be almost vertical, with lengths of approximately 2–3 μm (Figure 2c).

After surface modification with CoPi/Co(OH)₂, the surface morphology shows evidence of agglomeration of some nanorods (Figure 2b), suggesting that CoPi/Co(OH)₂ probably adsorbed on nanorod-arrays and caused them to bind together as shown in the marked areas. The corresponding cross-section morphology in Figure 2d shows similar features as the unmodified Ta₃N₅ nanorod-arrays in Figure 2c, and the nanorod agglomeration is not very clear.

Such nanorod-array structure should impart many merits like excellent conductivity and prominent quantum size effect, high specific surface area, and a large number of surface reaction sites, which will promote transport of electro-hole pairs. This means that solar energy conversion efficiency and light absorption ability will be enhanced, with the possibility of improved electrochemical protective performance.

3.2. Crystal Structure and Chemical Composition Analysis of Ta₃N₅

The XRD patterns of the as-prepared Ta₃N₅ material with and without CoPi/Co(OH)₂ modification are shown in Figure 3. When 2θ is at 17.21°, 19.74°, 24.47°, 26.00°, 30.09°, 33.85°, 34.49°, 36.01°, 38.68°, 43.67°, 46.67°, and 47.75°, the diffraction peaks are basically consistent with the standard Tantalum Nitride Ta₃N₅ (JCPDS card no. 19-1291). These peaks match with the (002), (021), (110), (111), (201), (025,) (401), and (025) crystal planes completely. The other weaker peaks include the Ta matrix and a small amount of tantalum nitride compounds of other valences arising from the nitriding treatment. A comparison of the modified and unmodified Ta₃N₅ materials reveals that the diffraction peak position and peak intensity of the two curves almost coincide. Moreover, no peaks are observed for CoPi/Co(OH)₂, indicating that their amounts may be too low to be detected

by XRD. This could also imply that the CoPi/Co(OH)$_2$ additives merely adhered to surface of the Ta$_3$N$_5$ nanorod-array, causing the observed agglomeration.
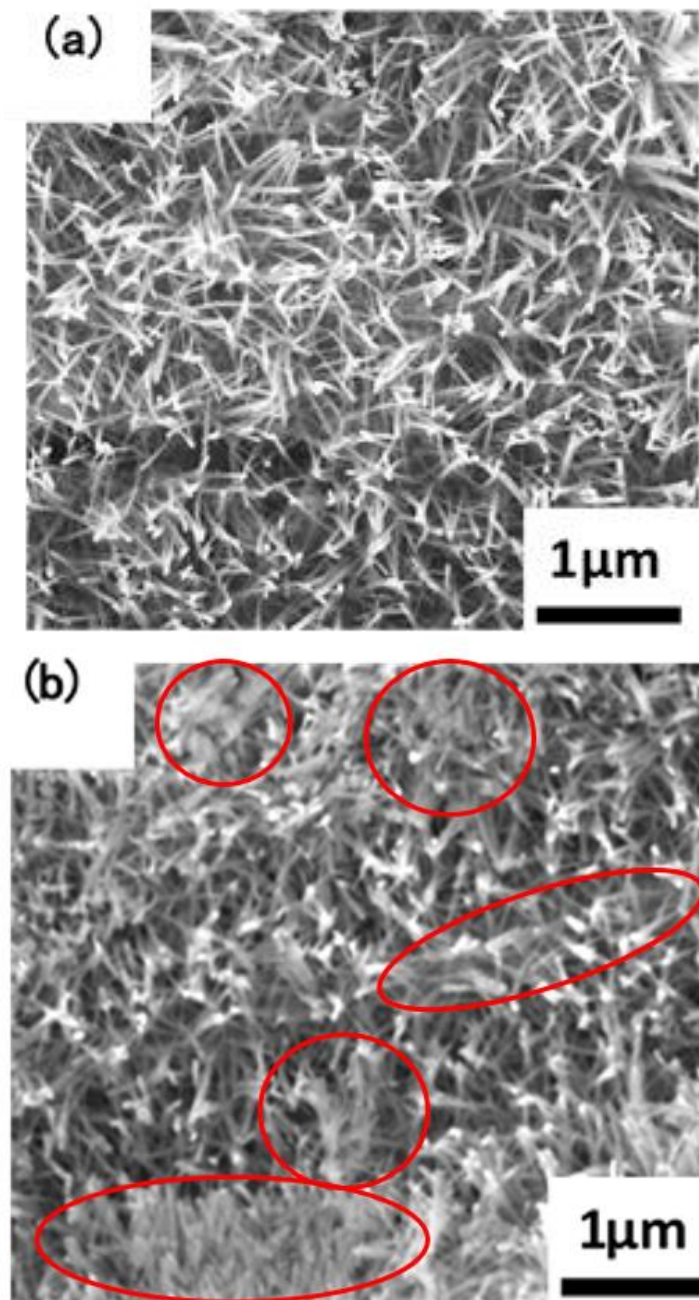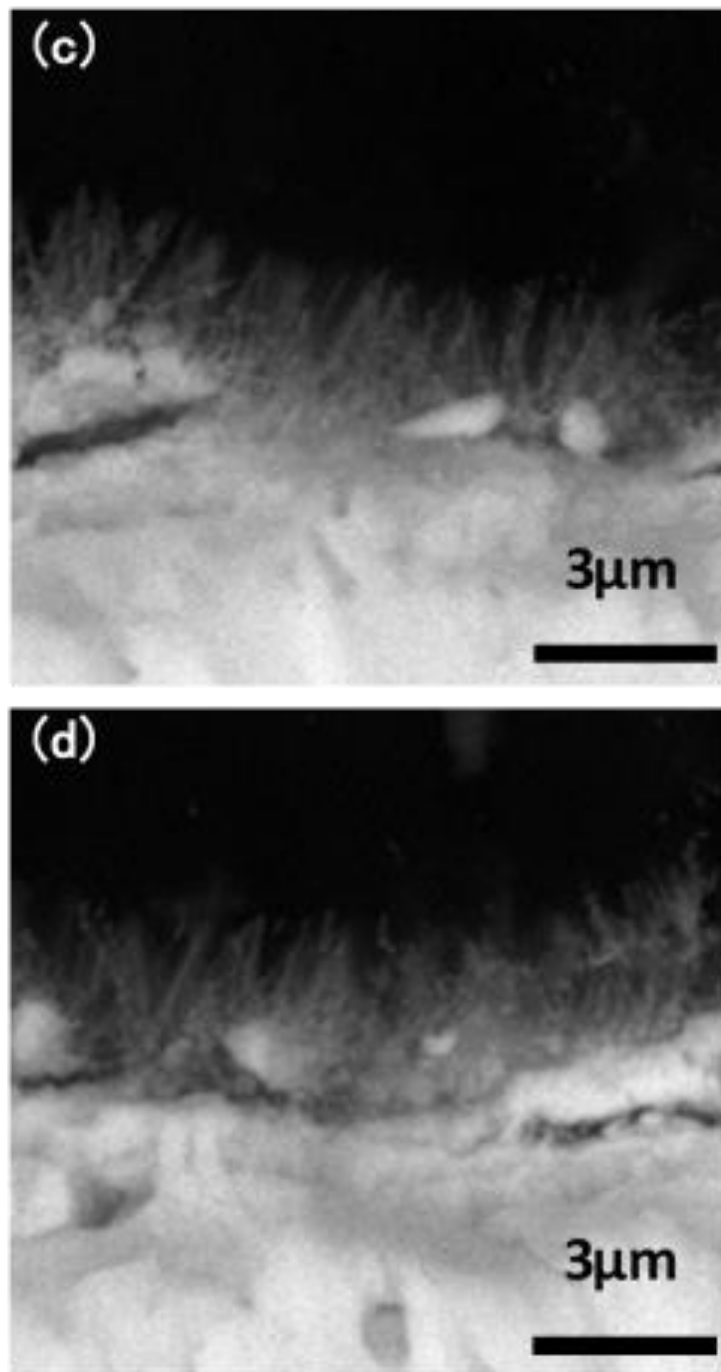

Figure 2. *Cont.*

Figure 2. SEM images of the microstructures of the prepared Ta_3N_5 nanorod-array films: (**a**) surface morphology of unmodified Ta_3N_5; (**b**) surface morphology of modified Ta_3N_5; (**c**) cross-section morphology of unmodified Ta_3N_5; (**d**) cross-section morphology of modified Ta_3N_5.

The compositions of the modified and unmodified Ta_3N_5 surfaces were further investigated by XPS, with special focus on the peaks and transformations of Co and P elements. The high-resolution complete survey XPS in Figure 4a shows Ta 4f, Ta 4d, N 1s, O 1s, Co 2p, and P 2p peaks, corresponding to the as-prepared samples. The major difference between the two curves is that the peak of the Co and P appeared only in the curve of the modified Ta_3N_5, indicating that $CoPi/Co(OH)_2$ was indeed successfully deposited on the surface of the Ta_3N_5 nanorod-array in the modified sample.
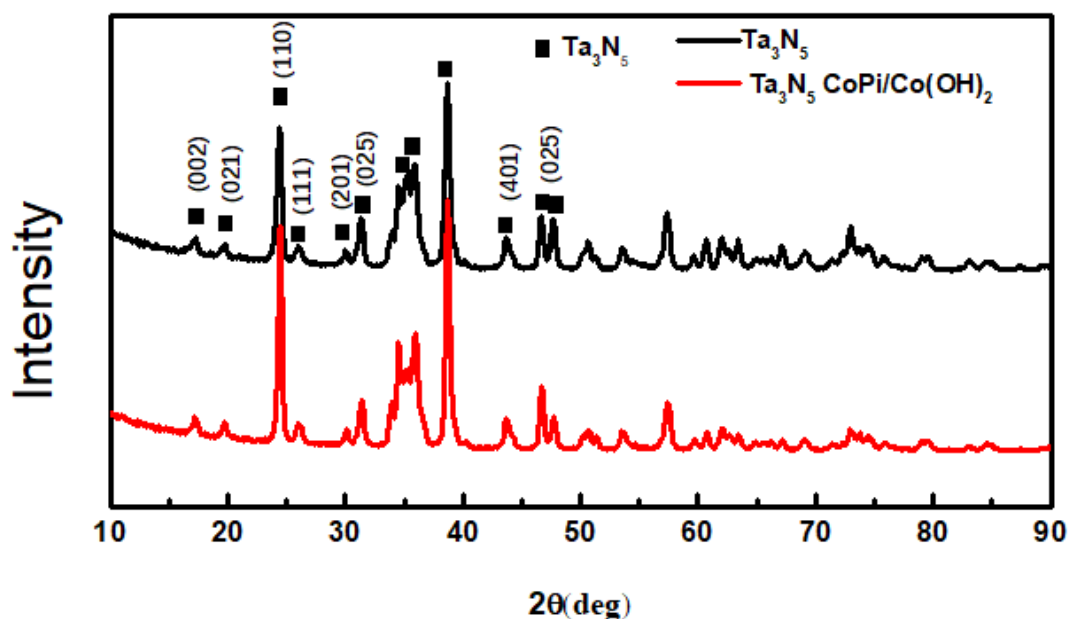
Figure 3. X-ray diffraction patterns of the Ta_3N_5 material with and without $CoPi/Co(OH)_2$ modification.

From the high-resolution spectra of $CoPi/Co(OH)_2$ for the modified Ta_3N_5 (Figure 4b), the binding energies of Co 2p3/2 and 2p1/2 (the red curve) are 780.0 eV and 795.6 eV, respectively. Furthermore, the peak of P 2p at 132.6 eV could be mainly attributed to the P element in CoPi in Figure 4c (the red curve). Both sets of results confirm the presence of $CoPi/Co(OH)_2$ on the modified Ta_3N_5.

3.3. UV-Vis Absorption Properties of Ta_3N_5

The UV-Vis diffuse reflectance spectrum of the Ta_3N_5 nanorod-array films with and without modification is shown in Figure 5. The absorption shoulders of both Ta_3N_5 curves are located deep into the visible region. The absorption spectra of the unmodified and $CoPi/Co(OH)_2$ modified Ta_3N_5 are 590 nm and 610 nm, respectively, corresponding to band gap energies ΔEg = 2.10 eV and 2.03 eV according to the equation $Eg = \frac{1240}{\lambda}$. The light absorption threshold of the $CoPi/Co(OH)_2$ surface-modified Ta_3N_5 is wider than the unmodified one, hence the narrowed band gap would result in lower photogenerated electron transition energy, stronger photocatalytic activity, and better photoelectric chemical protection performance in theory.

Ta_3N_5 is a new type of photocatalytic material with a broad spectral response range, which has a much higher visible absorption value and narrower energy gap than that of the TiO_2 photocatalyst. Hara et al. [22] reported the photocatalytic mechanism and energy band structure of TaON, Ta_2O_5, and Ta_3N_5 materials and ascribed the small energy gaps of TaON and Ta_3N_5 to the higher potential energy of the N 2p orbitals compared to the O 2p orbitals, resulting in the higher negative potential of Ta_3N_5 and the narrowing of the semiconductor energy gap.

3.4. Photoelectrochemical Cathodic Protection Performance of Ta_3N_5

After coupling of the Ta_3N_5 electrode (with or without $CoPi/Co(OH)_2$ modification) and the 304 stainless steel electrode, their open circuit potentials over time in 3.5 wt% NaCl solution in the dark and under the illumination were tested, as shown in Figure 6a. The duration of either cycle (in the dark and under the illumination) was 300 s, which means that a complete cycle lasted for 600 s.

The corrosion potential of the 304 stainless steel was initially determined to be approximately -0.17 V in 3.5 wt% NaCl solution by potentiodynamic polarization measurements. The unmodified Ta_3N_5 also has photocatalytic activity [23,24,39] and theoretically should generate some degree of

protective potential. However, the actual results in Figure 6a show that the potential of the unmodified Ta_3N_5 could only reach to -0.12 V after the first illumination (300 s). It remained stable under illumination and did not change with the continued illumination. This means that the OCP of the unmodified Ta_3N_5 (-0.12 V) is more positive than that of 304 stainless steel (-0.17 V). Therefore, the unmodified Ta_3N_5 cannot achieve electrochemical protection of 304 stainless steel.
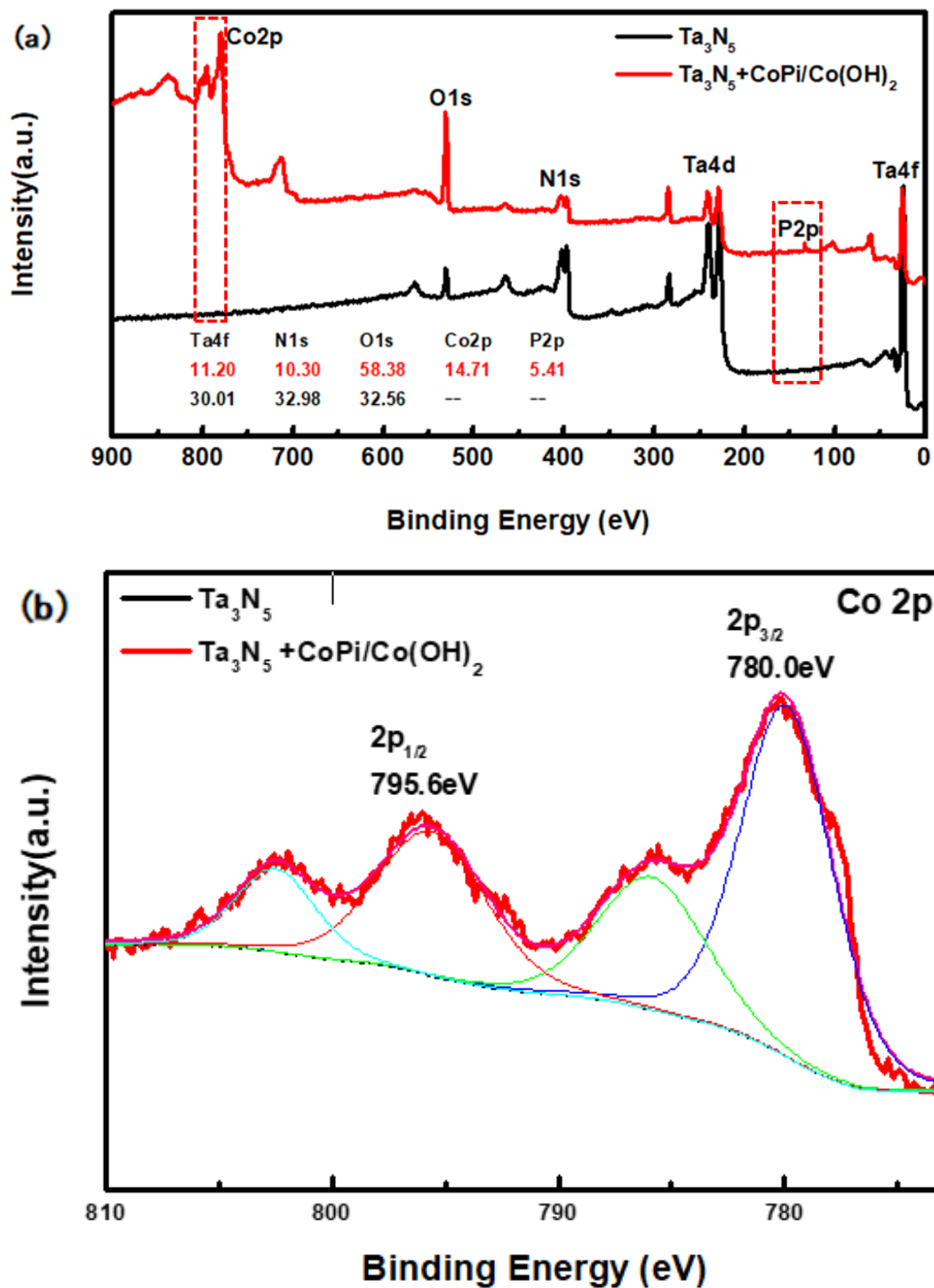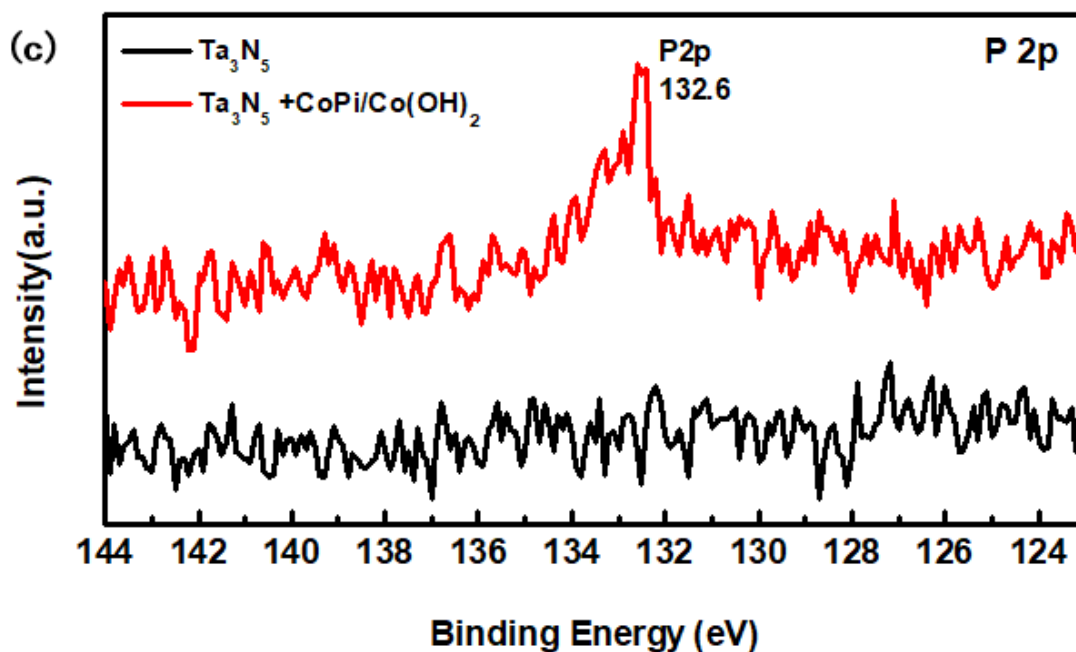

Figure 4. *Cont.*

Figure 4. X-ray photoelectron spectroscopy (XPS) spectra of the Ta_3N_5 material with and without $CoPi/Co(OH)_2$ modification: (**a**) survey spectrum, (**b**) Co 2p peak, (**c**) P 2p peak.
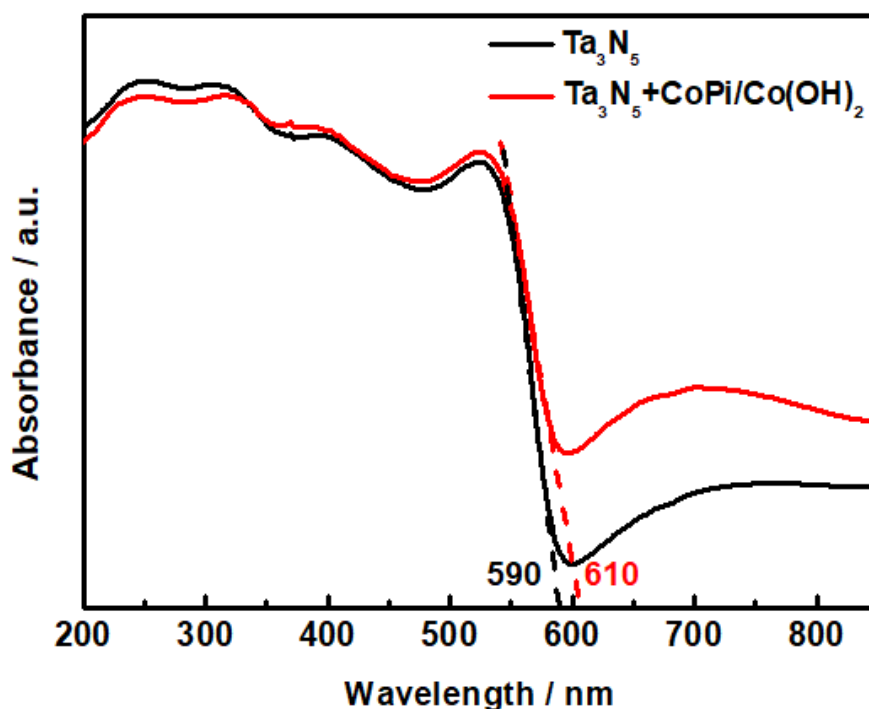

Figure 5. UV-Vis absorption spectra of the Ta_3N_5 material with and without $CoPi/Co(OH)_2$ modification.

For the Ta_3N_5 modified with $CoPi/Co(OH)_2$, the first photoinduced potential drop reached -0.45 V after 300 s, which is far lower (more cathodic) than the corrosion potential of 304 stainless steel, indicating that the generation and transfer of photogenerated electrons occurred instantaneously. Under this condition, there are no photogenerated holes to start reacting with OH^- and H_2O in solution, and the electrochemical protection of 304 stainless steel should be largely realizable. Although this

potential increases slowly to -0.20 V with prolonged illumination for 3000 s (at the end of illumination cycle), it still remained more negative than the corrosion potential of 304 stainless steel. Our results therefore prove that Ta_3N_5 modified with $CoPi/Co(OH)_2$ achieved photoelectrochemical cathodic protection of 304 stainless steel within the experimental time interval. However, the rising trend of its potential also indicates that $CoPi/Co(OH)_2$ is probably not stable and its ability to consume holes decreases on the surface of Ta_3N_5 nanorods. Ta_3N_5 material is also unstable and easy to be oxidized by photogenerated holes due to the accumulation of holes, so that its photoelectrochemical protective performance is still unstable.
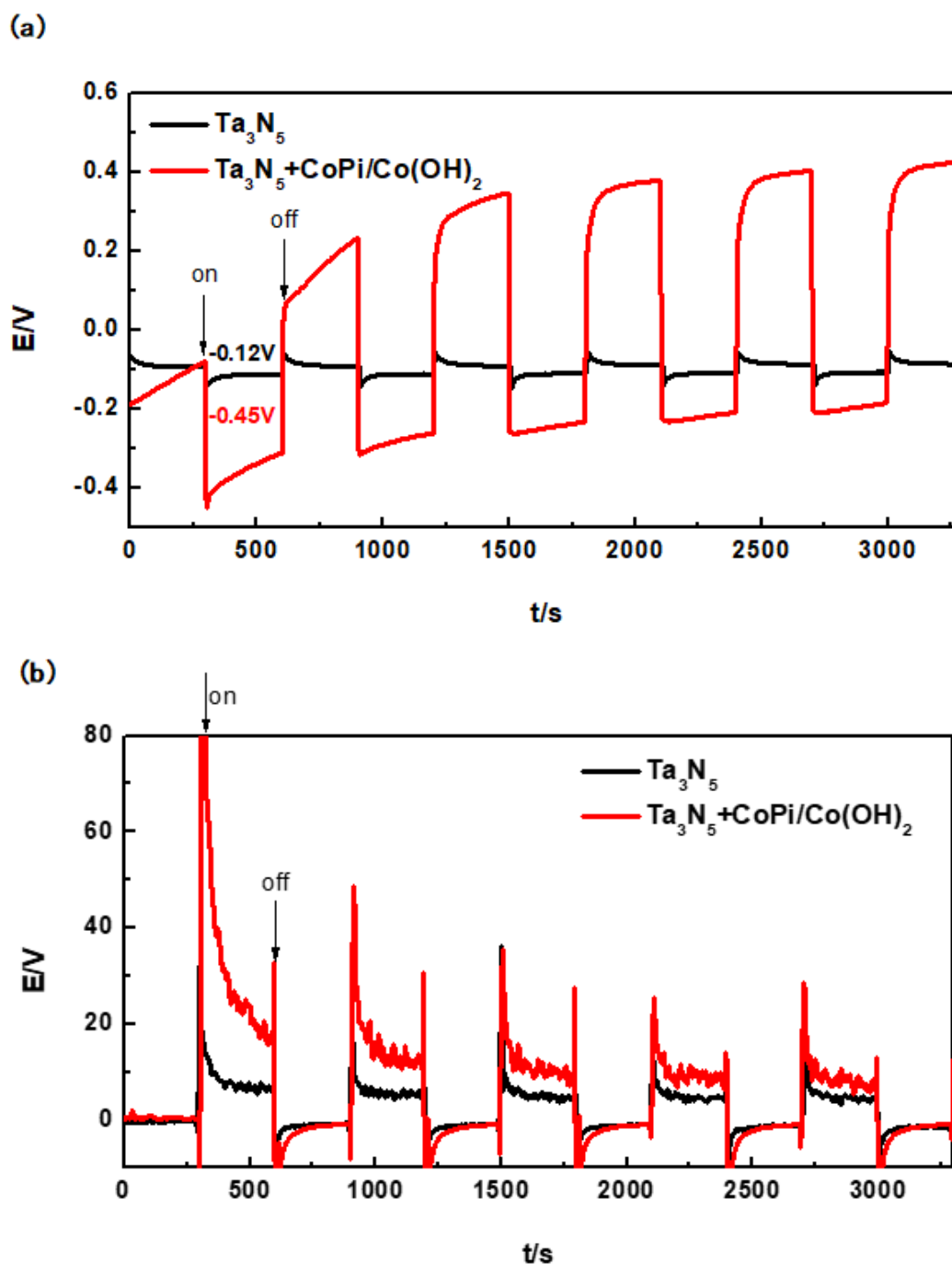

Figure 6. Evolution of open circuit potentials (**a**) and photocurrent densities (**b**) of modified and unmodified Ta_3N_5 material with and without illumination.

The minimum protection current density of 304 stainless steel is 15 µA/cm^2 [29]. As shown in Figure 6b, the instantaneous photocurrent of unmodified Ta$_3$N$_5$ can reach to 32 µA/cm^2 (300 s), but it remains stable at about 7 µA/cm^2 (600 s). This illustrates that the stable current cannot reach to 15 µA/cm^2, so that the 304 stainless steel cannot be protected, consistent with the change law of OCP.

There is an instantaneous rise to more than 80 µA/cm^2 that rapidly drops to 15 µA/cm^2 within one illumination cycle, and is just sufficient to protect 304 stainless steel within the first cycle. For subsequent cycles, the photocurrent density at the beginning of illumination consistently remained above 20 µA/cm^2, and then dropped to around 10 µA/cm^2 at the end of cycle. It is therefore obvious that CoPi/Co(OH)$_2$ modification improved the photocurrent of Ta$_3$N$_5$ consistent with the OCP results, and can thus be further investigated as a method for improving the performance of photocatalytic materials. Although the CoPi/Co(OH)$_2$ modified Ta$_3$N$_5$ does protect 304 stainless steel, the long-term performance would require further improvement.

3.5. Mechanism Analysis of Photoelectrochemical Cathodic Protection

The proposed mechanism of photoelectrochemical cathodic protection for 304 stainless steel under illumination by Ta$_3$N$_5$ modified with CoPi/Co(OH)$_2$ is schematically illustrated in Figure 7. Photogenerated electrons from the Ta$_3$N$_5$ valence band (VB) are excited to the conduction band (CB) under illumination, leaving photogenerated holes and electrons in the valence band and the conduction band, respectively. Subsequently, the photogenerated electrons transfer to the surface of the 304 stainless steel matrix to reduce oxygen, causing the surface potential of the 304 stainless steel to fall below its corrosion potential, thus realizing photoelectrochemical cathodic protection. At the same time, the photogenerated holes transfer from the VB to the CoPi/Co(OH)$_2$ additive to oxidize Co^{2+} into Co^{3+} [28].

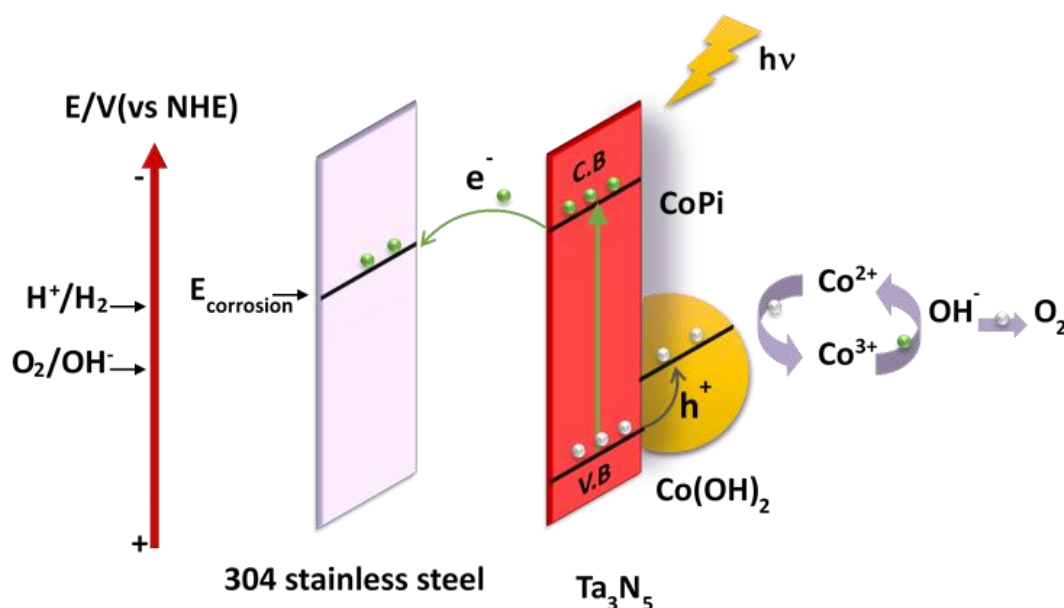**Figure 7.** Proposed mechanism of photoelectrochemical cathodic protection of 304 stainless steel by CoPi/Co(OH)$_2$ modified Ta$_3$N$_5$ films under illumination.

CoPi is strongly adsorbed on the surface of Ta$_3$N$_5$ and provides more adsorption sites and reaction sites in the reaction process. Co(OH)$_2$ is oxidized from Co^{2+} into Co^{3+}, and then the Co^{3+} oxidizes H$_2$O to O$_2$. During this process, Co^{3+} is reduced to Co^{2+}, which again awaits to be reoxidized by the next photogenerated hole. This cycle does not include Co^{2+} consumption. The valence transitions between Co^{2+} and Co^{3+} of the CoPi/Co(OH)$_2$ co-catalysis is favorable for separation and migration of photogenerated charges [33,40,41], and as a result, more holes are consumed, photogenerated charge

recombination and the reverse reaction is inhibited, and electron-hole pairs are increased [34,42,43]. Finally, the photostability and photogenerated electrons and holes utilization efficiency of Ta_3N_5 material are enhanced so that the protective effect on metals is improved.

4. Conclusions

The photoelectrochemical cathodic protection of 304 stainless steel in a 3.5 wt% NaCl solution by a novel broad-spectrum response material—CoPi/Co(OH)$_2$ modified Ta_3N_5—was studied. The main conclusions are as follows: CoPi/Co(OH)$_2$ modified Ta_3N_5 can attain a more negative corrosion potential and the minimum protection photocurrent density of 304 stainless steel and as such can theoretically achieve photoelectrochemical cathodic protection for 304 stainless steel. CoPi/Co(OH)$_2$, as co-catalyst, can reduce the activation energy of Ta_3N_5, promote photogenerated charge separation, consume holes and provide more active sites for electrochemical reactions, thus improving the photoelectric property and greatly enhancing the electrochemical protection for metals. However, long-term performance would require further improvement due to the decline of protection current density at the end of the later illumination cycles.

Conflicts of Interest: The authors declare no conflicts of interest.

References

1. Fujishima, H. Electrochemical photolysis of water at a semiconductor electrode. *Nature* **1972**, *238*, 37–38. [CrossRef] [PubMed]
2. Sun, M.; Chen, Z.; Bu, Y.; Yu, J.; Hou, B. Effect of ZnO on the corrosion of zinc, Q235 carbon steel and 304 stainless steel under white light illumination. *Corros. Sci.* **2014**, *82*, 77–84. [CrossRef]
3. Song, S.; Chen, Z. Effect of UV Illumination on the NaCl-Induced Atmospheric Corrosion of Pure Zinc. *J. Electrochem. Soc.* **2014**, *161*, C288–C293. [CrossRef]
4. Hasanov, R.; Bilge, S.; Bilgiç, S.; Gece, G.; Kılıç, Z. Experimental and theoretical calculations on corrosion inhibition of steel in 1M H_2SO_4 by crown type polyethers. *Corros. Sci.* **2010**, *52*, 984–990. [CrossRef]
5. Yuan, J.; Tsujikawa, S. Photo-Effects of Sol-Gel Derived TiO_2 Coating on Carbon Steel in Alkaline Solution. *Zairyo-to-Kankyo* **1995**, *44*, 534–542. [CrossRef]
6. Tatsuma, T.; Saitoh, S.; Ohko, Y.; Fujishima, A. TiO_2-WO_3 photoelectrochemical anticorrosion system with an energy storage ability. *Chem. Mater.* **2001**, *13*, 2838–2842. [CrossRef]
7. Wei, N.; Liu, Y.; Zhang, T.; Liang, J.; Wang, D. Hydrogenated TiO_2 nanotube arrays with enhanced photoelectrochemical property for photocathodic protection under visible light. *Mater. Lett.* **2016**, *185*, 81–84. [CrossRef]
8. Lin, Z.; Lai, Y.; Hu, R.; Li, J.; Du, R.; Lin, C. A highly efficient ZnS/CdS@TiO_2 photoelectrode for photogenerated cathodic protection of metals. *Electrochim. Acta* **2010**, *55*, 8717–8723. [CrossRef]
9. Brzezinska, M.; Garcia-Munoz, P.; Ruppert, A.M.; Keller, N. Photoactive ZnO Materials for Solar Light-Induced CuxO-ZnO Catalyst Preparation. *Materials (Basel)* **2018**, *11*, 2260. [CrossRef]
10. Hu, J.; Zhu, Y.-F.; Liu, Q.; Gao, Y.-B.; Du, R.-G.; Lin, C.-J. SnO_2 nanoparticle films prepared by pulse current deposition for photocathodic protection of stainless steel. *J. Electrochem. Soc.* **2015**, *162*, C161–C166. [CrossRef]
11. Pan, J.; Liu, G.; Lu, G.Q.; Cheng, H.M. On the true photoreactivity order of {001}, {010}, and {101} facets of anatase TiO_2 crystals. *Angew. Chem.* **2011**, *123*, 2181–2185. [CrossRef]
12. Liu, G.; Yang, H.G.; Pan, J.; Yang, Y.Q.; Lu, G.Q.; Cheng, H.M. Titanium dioxide crystals with tailored facets. *Chem. Rev.* **2014**, *114*, 9559–9612. [CrossRef]

13. Yang, J.; Yan, H.; Wang, X.; Wen, F.; Wang, Z.; Fan, D.; Shi, J.; Li, C. Roles of cocatalysts in Pt–PdS/CdS with exceptionally high quantum efficiency for photocatalytic hydrogen production. *J. Catal.* **2012**, *290*, 151–157. [CrossRef]

14. Bu, Y.; Chen, Z.; Li, W. Dramatically enhanced photocatalytic properties of Ag-modified graphene–ZnO quasi-shell–core heterojunction composite material. *RSC Adv.* **2013**, *3*, 24118–24125. [CrossRef]

15. Xie, Y.P.; Yu, Z.B.; Liu, G.; Ma, X.L.; Cheng, H.-M. CdS–mesoporous ZnS core–shell particles for efficient and stable photocatalytic hydrogen evolution under visible light. *Energy Environ. Sci.* **2014**, *7*, 1895–1901. [CrossRef]

16. Wang, X.; Wei, Q.; Zhang, L.; Sun, H.; Li, H.; Zhang, Q. CdTe/TiO$_2$ nanocomposite material for photogenerated cathodic protection of 304 stainless steel. *Mater. Sci. Eng. B* **2016**, *208*, 22–28. [CrossRef]

17. Wang, D.; Li, R.; Zhu, J.; Shi, J.; Han, J.; Zong, X.; Li, C. Photocatalytic Water Oxidation on BiVO4with the Electrocatalyst as an Oxidation Cocatalyst: Essential Relations between Electrocatalyst and Photocatalyst. *J. Phys. Chem. C* **2012**, *116*, 5082–5089. [CrossRef]

18. Li, S.; Zhang, L.; Wang, H.; Chen, Z.; Hu, J.; Xu, K.; Liu, J. Ta$_3$N$_5$-Pt nonwoven cloth with hierarchical nanopores as efficient and easily recyclable macroscale photocatalysts. *Sci. Rep.* **2014**, *4*, 3978. [CrossRef]

19. Wu, X.C.; Tao, Y.R.; Li, L.; Bando, Y.; Golberg, D. Centimeter-long Ta$_3$N$_5$ nanobelts: Synthesis, electrical transport, and photoconductive properties. *Nanotechnology* **2013**, *24*, 175701. [CrossRef]

20. Yokoyama, D.; Hashiguchi, H.; Maeda, K.; Minegishi, T.; Takata, T.; Abe, R.; Kubota, J.; Domen, K. Ta$_3$N$_5$ photoanodes for water splitting prepared by sputtering. *Thin Solid Films* **2011**, *519*, 2087–2092. [CrossRef]

21. Higashi, M.; Domen, K.; Abe, R. Fabrication of efficient TaON and Ta$_3$N$_5$ photoanodes for water splitting under visible light irradiation. *Energy Environ. Sci.* **2011**, *4*, 4138–4147. [CrossRef]

22. Hara, M.; Hitoki, G.; Takata, T.; Kondo, J.N.; Kobayashi, H.; Domen, K. TaON and Ta$_3$N$_5$ as new visible light driven photocatalysts. *Catal. Today* **2003**, *78*, 555–560. [CrossRef]

23. Luo, Y.; Liu, X.; Tang, X.; Luo, Y.; Zeng, Q.; Deng, X.; Ding, S.; Sun, Y. Gold nanoparticles embedded in Ta$_2$O$_5$/Ta$_3$N$_5$ as active visible-light plasmonic photocatalysts for solar hydrogen evolution. *J. Mater. Chem. A* **2014**, *2*, 14927–14939. [CrossRef]

24. Zhen, C.; Wang, L.; Liu, G.; Lu, G.Q.; Cheng, H.M. Template-free synthesis of Ta$_3$N$_5$ nanorod arrays for efficient photoelectrochemical water splitting. *Chem. Commun.* **2013**, *49*, 3019–3021. [CrossRef] [PubMed]

25. Xu, H.; Li, S.; Ge, L.; Han, C.; Gao, Y.; Dai, D. In-situ synthesis of novel plate-like Co(OH) 2 co-catalyst decorated TiO 2 nanosheets with efficient photocatalytic H 2 evolution activity. *Int. J. Hydrogen Energy* **2017**, *42*, 22877–22886. [CrossRef]

26. Liu, H.; Xue, Q.; Zhao, J.; Zhang, Q. Enhanced supercapacitive performance of binary cooperative complementary Co(OH)$_2$/Mn$_3$O$_4$ nanomaterials directly synthesized through ion diffusion method controlled by ion exchange membrane. *Electrochim. Acta* **2018**, *260*, 330–337. [CrossRef]

27. An, Y.; Xu, B.; Liu, Y.; Wang, Z.; Wang, P.; Dai, Y.; Qin, X.; Zhang, X.; Huang, B. Photocatalytic Overall Water Splitting over MIL-125(Ti) upon CoPi and Pt Co-catalyst Deposition. *ChemistryOpen* **2017**, *6*, 701–705. [CrossRef]

28. Wang, P.; Xu, S.; Xia, Y.; Wang, X.; Yu, H.; Yu, J. Synergistic effect of CoPi-hole and Cu(ii)-electron cocatalysts for enhanced photocatalytic activity and photoinduced stability of Ag$_3$PO$_4$. *Phys. Chem. Chem. Phys.* **2017**, *19*, 10309–10316. [CrossRef]

29. Xie, X.; Liu, L.; Chen, R.; Liu, G.; Li, Y.; Wang, F. Long-Term Photoelectrochemical Cathodic Protection by Co(OH)$_2$-Modified TiO$_2$ on 304 Stainless Steel in Marine Environment. *J. Electrochem. Soc.* **2018**, *165*, H3154–H3163. [CrossRef]

30. Wang, L.; Dionigi, F.; Nguyen, N.T.; Kirchgeorg, R.; Gliech, M.; Grigorescu, S.; Strasser, P.; Schmuki, P. Tantalum Nitride Nanorod Arrays: Introducing Ni–Fe Layered Double Hydroxides as a Cocatalyst Strongly Stabilizing Photoanodes in Water Splitting. *Chem. Mater.* **2015**, *27*, 2360–2366. [CrossRef]

31. Hutchings, G.S.; Zhang, Y.; Li, J.; Yonemoto, B.T.; Zhou, X.; Zhu, K.; Jiao, F. In situ formation of cobalt oxide nanocubanes as efficient oxygen evolution catalysts. *J. Am. Chem. Soc.* **2015**, *137*, 4223–4229. [CrossRef] [PubMed]

32. Irshad, A.; Munichandraiah, N. An oxygen evolution Co-Ac catalyst–the synergistic effect of phosphate ions. *Phys. Chem. Chem. Phys.* **2014**, *16*, 5412–5422. [CrossRef] [PubMed]

33. Qorbani, M.; Naseri, N.; Moshfegh, A.Z. Hierarchical Co3O4/Co(OH)2Nanoflakes as a Supercapacitor Electrode: Experimental and Semi-Empirical Model. *ACS Appl. Mater. Interfaces* **2015**, *7*, 11172–11179. [CrossRef] [PubMed]

34. Zhang, G.; Zang, S.; Wang, X. Layered Co(OH)$_2$ Deposited Polymeric Carbon Nitrides for Photocatalytic Water Oxidation. *ACS Catal.* **2015**, *5*, 941–947. [CrossRef]

35. Sun, M.; Chen, Z.; Bu, Y. Enhanced photoelectrochemical cathodic protection performance of the C$_3$N$_4$@In$_2$O$_3$ nanocomposite with quasi-shell–core structure under visible light. *J. Alloys Compd.* **2015**, *618*, 734–741. [CrossRef]

36. Wang, W.; Wang, X.; Wang, N.; Ning, X.; Li, H.; Lu, D.; Liu, X.; Zhang, Q.; Huang, Y. Bi$_2$Se$_3$ Sensitized TiO$_2$ Nanotube Films for Photogenerated Cathodic Protection of 304 Stainless Steel Under Visible Light. *Nanoscale Res. Lett.* **2018**, *13*, 295. [CrossRef] [PubMed]

37. Zhang, H.; Li, Y.; Liu, P.; Li, Y.; Yang, D.; Yang, H.; Zhao, H. A new vapor-phase hydrothermal method to concurrently grow ZnO nanotube and nanorod array films on different sides of a zinc foil substrate. *Chemistry* **2012**, *18*, 5165–5169. [CrossRef] [PubMed]

38. Liu, P.; Zhang, H.; Liu, H.; Wang, Y.; Yao, X.; Zhu, G.; Zhang, S.; Zhao, H. A Facile Vapor-Phase Hydrothermal Method for Direct Growth of Titanate Nanotubes on a Titanium Substrate via a Distinctive Nanosheet Roll-Up Mechanism. *J. Am. Chem. Soc.* **2011**, *133*, 19032–19035. [CrossRef]

39. Feng, X.; Latempa, T.J.; Basham, J.I.; Mor, G.K.; Varghese, O.K.; Grimes, C.A. Ta$_3$N$_5$ nanotube arrays for visible light water photoelectrolysis. *Nano Lett.* **2010**, *10*, 948–952. [CrossRef]

40. Nellist, M.R.; Laskowski, F.A.L.; Qiu, J.; Hajibabaei, H.; Sivula, K.; Hamann, T.W.; Boettcher, S.W. Potential-sensing electrochemical atomic force microscopy for in operando analysis of water-splitting catalysts and interfaces. *Nat. Energy* **2018**, *3*, 46. [CrossRef]

41. Yang, J.; Wang, D.; Han, H.; Li, C. Roles of cocatalysts in photocatalysis and photoelectrocatalysis. *Acc. Chem. Res.* **2013**, *46*, 1900–1909. [CrossRef] [PubMed]

42. Tao, F.; Shen, Y.; Liang, Y.; Li, H. Synthesis and characterization of Co(OH)$_2$/TiO$_2$ nanotube composites as supercapacitor materials. *J. Solid State Electrochem.* **2006**, *11*, 853–858. [CrossRef]

43. Hou, J.; Wang, Z.; Yang, C.; Cheng, H.; Jiao, S.; Zhu, H. Cobalt-bilayer catalyst decorated Ta$_3$N$_5$ nanorod arrays as integrated electrodes for photoelectrochemical water oxidation. *Energy Environ. Sci.* **2013**, *6*, 3322–3330. [CrossRef]